FLOW **CAMBRIDGE**
UNIVERSITY PRESS

RESEARCH ARTICLE

Turbulence-induced electrical discharges in charged particle-laden Martian boundary layers

Mustafa Mutiur Rahman[1,2,*] (iD), Ahmed Saieed[1] (iD) and Jean-Pierre Hickey[1,*] (iD)

[1]Department of Mechanical and Mechatronics Engineering, University of Waterloo, Waterloo, Ontario N2L 3G1, Canada
[2]Scalable Solvers Group, Applied Mathematics and Computational Research Division, Lawrence Berkeley National Laboratory, Berkeley, CA 94720, USA
*Corresponding authors. E-mail: mustafa.rahman@kaust.edu.sa; jean-pierre.hickey@uwaterloo.ca

Abstract

Martian dust storms in the planetary boundary layer share many qualitative similarities to terrestrial sandstorms. Both of these turbulence-driven, particle-laden boundary layer flows are known to generate electric fields due to the transport of differentially charged particles; this charge separation can be strong enough to lead to dielectric breakdown in the form of sparks or lightning. Using wall-modelled large-eddy simulations supplemented with conservation of equations for the charged particle transport, representative simulations of neutrally stable Martian and terrestrial particle-laden boundary layer flows are compared. The simulations, albeit canonical in nature, provide evidence to support previous observations of the less frequent occurrence of lightning on Mars but a higher occurrence of localised electric discharge events due to the much lower breakdown potential. The rarefied Martian atmosphere impedes charged particle transport, resulting in a weaker electric field than the equivalent terrestrial sandstorm. The lower drag force in the rarefied Martian atmosphere means that the electrostatic force plays a more significant role in the particle transport, which results in a self-regulation of the electric field. The strongest Martian dust storms show evidence of significant breakdown events and these discharge events only occur very close to the ground despite the very large boundary layer on Mars.

Impact Statement

Martian dust storms share many qualitative similarities to terrestrial sandstorms. Electrically charged particles of different sizes are transported by turbulence, which results in charge separation and the generation of electric fields. Lightning is a common occurrence on Earth, yet has been shown to occur less frequently on Mars. The lower breakdown potential of the Martian atmosphere gives rise to a higher probability of discharge events without large-scale lightning. Using high-fidelity simulations of representative Martian and terrestrial planetary boundary layers, we show that the turbulent particle transport on Mars is impeded due to rarefied atmosphere. Mars shows a high occurrence of local dielectric breakdown but no large-scale lightning as observed on Earth.

1. Introduction

Storms and atmospheric winds are a common occurrence on any planetary body possessing an atmosphere. An elementary characteristic of such fluidic motion is the entrainment of surface particles, which collide at the mercy of boundary layer turbulence; this occurs on numerous planets, such as Mars, despite a much lower atmospheric pressure and density than on Earth (Burr et al., 2020). Although the physical mechanism driving the particle saltation is a subject of active research with many open questions (Kok & Renno, 2006; Kruss et al., 2021; Pähtz, Clark, Valyrakis, & Durán, 2020), the occurrence of dust clouds and storms on Mars is indubitable. On Mars, these dust storms represent thermodynamically important climatology events that modulate the circulation patterns through a substantial warming of the Martian atmosphere (Bertrand, Wilson, Kahre, Urata, & Kling, 2020). The atmospheric dust particles also present a significant challenge to any space mission. For these reasons, Martian dust storms have and continue to receive much warranted scientific attention.

As these particles collide and interact close to the ground, triboelectric effects result in the particles becoming differentially charged (Duff & Lacks, 2008) – larger-sized particles become positively charged, while smaller-sized dust grains take on a negative charge. Forward, Lacks, and Sankaran (2009) argue that as particles collide, the valence electrons of one particle move to a lower energy state on the second particle. Thus, in a collision, the larger particles lose electrons and become positively charged, whereas smaller particles acquire these electrons and become negatively charged. As these particles of different masses are differentially entrained by the atmospheric boundary layer turbulence, charge separation arises and results in the creation of large self-sustaining electric fields of over 100 kV m^{-1} (Kok & Renno, 2006). Locally, charge separation can also arise due to preferential clustering (Di Renzo & Urzay, 2018) – in both laboratory (Cimarelli, Alatorre-Ibargüengoitia, Kueppers, Scheu, & Dingwell, 2014) and field experiments (Zhang & Zhou, 2020) – and orientation of non-spherical particles (Lee, Waitukaitis, Miskin, & Jaeger, 2015; Mallios, Daskalopoulou, & Amiridis, 2021; Waitukaitis, Lee, Pierson, Forman, & Jaeger, 2014).

The charge separation can be sufficiently strong to create dielectric breakdown events that can be observed as localised sparks or large-scale lightning. Lightning is a common occurrence on Earth in turbulent particle clouds resulting from volcanic eruptions or desert sandstorms (Rahman, Cheng, & Samtaney, 2021). Lightning has also been observed in Martian dust storms, although clear experimental evidence remains elusive (see Izvekova, Popel, and Izvekov (2022) and references therein). On Mars, the arid atmospheric conditions, the large-scale atmospheric winds, and the compositional (large iron oxide content (Sobrado, Martín-Soler, & Martín-Gago, 2015)) make-up of these micrometre-sized particles are well suited to generate strong electric fields. The electric field and spark discharge events have been shown to alter the chemical composition of the Martian atmosphere (Kok & Renno, 2009), while simultaneously hindering communication and damaging sensitive electronic equipment for spatial exploration missions (Zhou, He, & Zheng, 2005). Spark discharge events arise when the charge separation reaches the ambient atmospheric breakdown potential (Jackson & Farrell, 2006). The dielectric breakdown potential on Mars is around 20–25 kV m^{-1}, less than one per cent of Earth's breakdown potential (Melnik & Parrot, 1998; Zhai, Cummer, & Farrell, 2006). This suggests that electric discharge events may occur more readily on Mars, although some experimental work suggests that large-scale discharge events such as lightning may, in fact, be less frequent and not as strong as on Earth (Wurm, Schmidt, Steinpilz, Boden, & Teiser, 2019). In fact, Anderson et al. (2011) reported no observable lightning events over a three-month observation window of Mars. This is despite the fact that triboelectrific spark discharges have been shown to readily occur using a dust simulant under representative Martian conditions (Harper, Dufek, & McDonald, 2021).

Planetary boundary layer (PBL) turbulence, through the entrainment of the differentially charged particles, is the key to understanding the prevalence of large-scale lightning events in these particle-laden flows. Rahman et al. (2021) conducted large-eddy simulations (LES) of charged particle-laden turbulent layer of terrestrial sandstorms. They showed an overall drop in the electric field with elevation; findings that were supported by the results of Zhang, Zheng, and Bo (2014) and Kok and Renno (2008).

It should be noted that the altitude of a dust storm is primarily determined by the turbulent boundary layer, and thus represents a crucial parameter. Although the measured turbulence statistics and spectra of the PBL on Mars and Earth share many similarities (Banfield et al., 2020; Chen, Lovejoy, & Muller, 2016; Temel et al., 2022), the resulting Martian storms reach much higher altitudes than their terrestrial counterparts; these dust storms form cloud-like patterns similar to those on Earth (Sánchez-Lavega et al., 2022). Also, the atmospheric turbulence responsible for the transport of dust particles is more heavily modulated by the stronger diurnal variations and radiative surface forcing on Mars; the transport of dust at very high altitudes is hypothesised to be governed by large-scale dust devils (Izvekova & Popel, 2017). It has even been suggested that dust particles can enhance the boundary layer turbulence on Mars due to convective effects (Spiga, 2021; Wu et al., 2021). Therefore, the quantification of the breakdown events caused by terrestrial sandstorms cannot be directly extended to Martian storms – especially when considering the drastic differences in thermophysical properties and breakdown potential of both these atmospheres. Hence, even though the Martian atmosphere has been the subject of intensive research (Harper et al., 2021; Laurent, Tobias, Jens, & Gerhard, 2021; Mallios et al., 2021; Witze, 2021), there are some fundamental scientific questions that are still unanswered with respect to the role of turbulence on charge separation and discharge events.

On the basis of the above discussion, the objective of this work is to elucidate and quantify the role of turbulence on the large-scale electric field generation and discharge events in Martian dust storms in order to compare and contrast the findings from terrestrial sandstorms. Very few works have simulated representative Martian boundary layer flows (although we do note recent work by Temel et al. (2021) and Wu et al. (2021)) but, to the knowledge of the authors, no work has focused on the charged particle-laden PBL to understand the implications on charge separation. This work differs from Di Renzo and Urzay (2018), in that preferential concentration is not the dominant mechanism of charge separation, as was shown to be the case in forced isotropic turbulence. Here, the charge separation stems from the concentration differences in the wall normal direction, which can induce large-scale charge separation in PBL flows. Although the present canonical set-up avoids many of the specific challenges in the Martian PBL (radiative forcing, thermal stratification, particle transport due to dust devils, baroclinic vortices, etc.), it isolates the effects of turbulence on the transport of these charged particles at conditions that are relevant to Mars.

2. Methodology

We develop a mathematical model of electrified, particle-laden PBL to understand the role of turbulence in charge separation and, ultimately, dielectric breakdown at conditions that are relevant to the Martian atmosphere. Given the very large-scale separation in these PBL, wall-modelled large-eddy simulations (WMLES) of representative particle-laden turbulent atmospheric flow are conducted following the work of Rahman et al. (2021). The multiphase numerical framework is based on an Eulerian–Eulerian approach and solves the incompressible Navier–Stokes equations along with the conservation of equations for the charged particles.

Considering the present particle size (see table 1), the choice of an Eulerian approach for the dispersed phase might seem questionable (Balachandar & Eaton, 2010). Firstly, the employed WMLES coupled with a direct quadrature moment method (DQMOM) provides a robust framework for this analysis as the DQMOM method is known for handling particle-laden flows effectively. Secondly, figure 1 plots the representative time scales and length scales for varying mesh resolutions of our LES simulations. Due to the very large Reynolds number, it can be observed from the plot that most of the particles lie in the equilibrium–Eulerian range. Even though the equilibrium–Eulerian approach seems reasonable, the Eulerian approach is more conservative as it can take account of the electrostatic force. Guided from the plot and classifications of Balachandar and Eaton (2010) (provided in their figure 1), it is reasonable to adopt the Eulerian description of the approach for the particulate phase of the representative PBL. Hence, both carrier and dispersed phases are considered as a continuum occupying the same region in space.

Table 1. *Comparison of parameters for Martian and terrestrial environments. The references for each of our selected parameters are discussed in the text.*

	Martian	Terrestrial
Atmosphere	Rarefied, CO_2 rich	N_2, O_2 rich
Breakdown voltage (E_T)	25 kV m^{-1}	3 MV m^{-1}
Pressure (p)	6.9 mbar	1 bar
Density of atmosphere (ρ_f)	1.6×10^{-2} kg m^{-3}	1.225 kg m^{-3}
Dynamic viscosity (μ)	1.3×10^{-5} Nsm^{-2}	1.8×10^{-5} Nsm^{-2}
Kinematic viscosity (ν)	8.1×10^{-4} m^2 s^{-1}	1.48×10^{-5} m^2 s^{-1}
Boundary layer (δ)	6000 m	1000 m
Velocity (U_∞)	13.5 m s^{-1}	15 m s^{-1}
Reynolds number (Re_δ)	10^8	10^9
Particle sizes (d_s)	(200, 600) μm	(200, 500) μm
Particle density (ρ_s)	(3200, 3200) kg m^{-3}	(2650, 2650) kg m^{-3}
Particle charge (q_s)	(-4, 2.24) fC	(-4, 2.24) fC
Base concentration (n_{b1}, n_{b2})	(2×10^7, 3.4×10^6) m^{-3}	(2×10^7, 3.4×10^6) m^{-3}
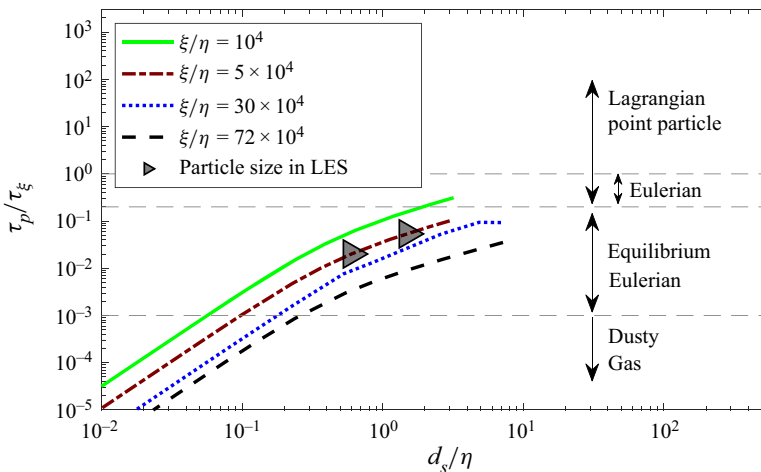
Figure 1. *The plot comparing the typical simulation conditions of sandstorms for low Reynolds number ($Re = 10^8$) and high-resolution conditions ($\xi/\eta = 10\,000$) with high Reynolds number ($Re = 2 \times 10^9$) and low resolution ($\xi/\eta = 720\,000$) simulation parameters from Balachandar and Eaton (2010). Here ξ is the smallest resolved scale.*

The relative importance of the hydrodynamic forces in the particle-laden flows can be characterised by representative non-dimensional quantities. The most important is the Stokes number which relates the particle time scale ($\tau_p = \rho_p d_p^2 / 18\mu\rho_f$) to the relevant turbulence time scale (τ_f) (Crowe, Gore, & Troutt, 1985):

$$St = \frac{\tau_p}{\tau_f}. \tag{2.1}$$

The fluid time scale, τ_f, is often taken as the local Kolmogorov time scale of the turbulence. In the above equation, subscripts p and f stand for particle and carrier fluid, respectively. While, ρ and μ are the density and dynamic viscosity.

In this work, we utilise the physical characteristics of the terrestrial and Martian atmosphere and representative dust particles to develop phenomenological models to simulate dust storms in a PBL. The present particle model is predicated on the following assumptions: (*a*) collisions and triboelectric charging between particles occurs in a very thin layer close to the ground; (*b*) the small and large particles carry an opposite electric charge; and (*c*) these bidispersed, charged particles are entrained and preferentially distributed by the boundary layer turbulence. The turbulent transport of these particles results in a charge separation, and ultimately, dielectric breakdown events if the breakdown potential is reached. The particles are one-way coupled in momentum with the surrounding fluid (with particle mass loading ratio of less than 0.1 only the carrier fluid exerts a drag force on the particles), whereas the particles interact with each other via long-range Coulomb interactions. We note that other works also include short-range Coulomb interactions, which are not included herein (Di Renzo & Urzay, 2018; Zhang, Cui, & Zheng, 2023).

The particle concentration is imposed as a Dirichlet boundary condition that is constant over time. The imposition of a constant Dirichlet boundary condition for the particle concentration serves as a practical approximation that simplifies the representation of real-world conditions. This approach is adopted due to practical constraints and the inherent characteristics of sand deposition processes. Firstly, in sandstorm simulations, the ground is typically considered a fixed and stationary surface that acts as a source or sink for sand particles. By imposing a constant particle concentration at the ground, the model assumes that the sediment source or sink remains relatively stable over time and does not vary significantly during the simulated period. This assumption is reasonable for sandstorm scenarios where the sediment source, such as a desert or a specific region, is not expected to undergo rapid and significant changes. By imposing a constant Dirichlet boundary condition for the particle concentration at the ground, the model assumes that the particle accumulation has reached a quasisteady state, where the concentration remains relatively constant over time. This assumption is reasonable because the deposition and resuspension processes in sandstorm flows occur over longer time scales compared with the temporal variations of the flow itself. Secondly, considering the practical limitations of data collection and measurements near the ground, it is often challenging to obtain accurate and continuous temporal profiles of particle concentration at the ground level in real-world sandstorm events. By imposing a constant Dirichlet boundary condition, the model provides a simplification that allows for a more tractable and computationally efficient representation of the sandstorm flow. This simplification reduces the complexity of the model and enables more practical and feasible simulations. Thirdly, the constant Dirichlet boundary condition simplifies the computational implementation and numerical stability of the sandstorm model. In numerical simulations, it is often beneficial to prescribe a fixed boundary condition that does not vary with time to ensure a well-posed problem and facilitate accurate and efficient calculations. It is worth noting that the constant Dirichlet boundary condition for the particle concentration at the ground is a simplifying assumption, and in reality, the concentration may exhibit spatial and temporal variations near the surface due to factors such as wind gusts, local topography and particle resuspension events. However, for the purpose of capturing the overall behaviour and essential characteristics of multiphase sandstorm flows, the constant boundary condition serves as a reasonable approximation. In summary, the imposition of a constant Dirichlet boundary condition for the particle concentration at the ground in the modelling of multiphase sandstorm flows is justified by the quasisteady state assumption of particle accumulation near the surface and the practical limitations of data collection. Although it simplifies the representation of the flow, it provides a reasonable approximation for capturing the essential features of sand deposition processes in sandstorm simulations.

2.1. *Characteristics of terrestrial and Martian PBL*

Before presenting the modelling aspects, it is important to understand the characteristics of PBL on both planets, which are discussed below.

2.1.1. Terrestrial PBL

During dust storms on Earth, the PBLs can exhibit a wide range of scales depending on various factors such as the intensity of the dust storm, the local atmospheric conditions and the topography of the region. However, it is possible to provide a typical range for streamwise velocity and turbulence intensity based on International Standard Atmosphere (ISA) conditions (with standard temperature as 15 °C, standard pressure is 1 atm, and without humidity) having dynamic viscosity (μ) of 1.88×10^{-5} Pa s, the kinematic viscosity of air (ν) of 1.5×10^{-5} m^2 s^{-1} and density of air as 1.25 kg m^{-3}.

In the PBL during dust storms on Earth, the streamwise velocity can vary significantly depending on the local conditions. However, based on measurements and simulations, typical values of streamwise velocity in neutrally stable terrestrial PBL during a dust storm can range from a few to tens of metres per second. We have considered wind speeds of 15 m s^{-1} and the turbulent boundary layer of 1 km, as in the works of Calaf, Meneveau, and Meyers (2010).

Turbulence intensity refers to the fluctuation of wind velocity in the PBL. During dust storms, the turbulence intensity can increase due to the presence of strong winds and turbulent mixing. While turbulence intensity can vary depending on the specific conditions, studies have reported turbulence intensities ranging roughly from 10 % to 40 % during dust storms close to the Earth's surface (Kaimal & Finnigan, 1994).

2.1.2. Martian PBL

On Mars, dust storms can have a significant impact on the Martian PBL, which behaves differently from Earth's PBL due to the differences in atmospheric conditions and terrain. Mars has a much thinner atmosphere compared with Earth, with a density (ρ_f) of 1.6×10^{-2} kg m^{-3}, resulting in lower wind speeds. However, during dust storms on Mars, the streamwise velocity can increase significantly. Typical streamwise velocities during Martian dust storms can range from a few metres per second to approximately 20 m s^{-1}; we opted to use 13.5 m s^{-1} as the free stream velocity. We have considered an atmospheric boundary layer height of 6 km, as in Haberle, Clancy, Forget, Smith, and Zurek (2017).

Due to the lower density on Mars, turbulence intensity is generally lower compared with Earth because of the lower Reynolds number. However, during dust storms, turbulence intensity can still increase due to turbulent mixing and the interaction of the dust particles with the atmosphere. Turbulence kinetic energy in the Martian PBL can take a wide range of values (Wu et al., 2021).

2.2. Modelling dust storms

Considering the discussion above, neutrally stable simulations are run at representative conditions of the Martian and terrestrial PBL based on the characteristics found in the literature, as discussed here and summarised in table 1. For all the simulation cases reported here, we fix the free stream velocity on Mars (Earth) to $U_\infty = 13.5$ m s^{-1} (15 m s^{-1}) and a boundary layer height of $\delta = 6000$ m (1000 m) (Calaf et al., 2010). The kinematic viscosity of atmospheric gas is selected as 8.1×10^{-4} m^2 s^{-1} (1.5×10^{-5} m^2 s^{-1}) (Haberle et al., 2017). The atmospheric pressure on Mars is set to 6.9 mbar which is close to the measured atmospheric pressure in a number of studies (Haberle et al., 2017). The corresponding Reynolds number based on the boundary layer thickness is $Re_\delta = 10^8$ ($=10^9$). Given the incompressible nature of the simulations, the primary difference between the terrestrial and Martian PBLs herein lies in the inner wall and outer wall scaling relations and Reynolds number, as well as the drag force on the particle (due to the lower viscosity and density). We sample the distribution of the particle number density function at two points ($S = 2$), in other words, two different particle sizes are considered: $d_1 = 200\,\mu$m ($d_1 = 200\,\mu$m) with negative charge and $d_2 = 600\,\mu$m ($d_2 = 500\,\mu$m) with positive charge. Although fine dust represents a significant portion of the solid phase transport in these particle-laden PBLs, the larger-sized particles contribute more readily to the charge separation and thus are considered here. The selected particles represent a reasonable choice given the wide particle size distribution found on both planets. The particles have a density of 3200 kg m^{-3} (2650 kg m^{-3}). The representative (ideal) electric charge of the species of each size is $Q_1 \equiv (q_1, q_2) = (-4 \times 10^{-15}\,\text{C}, 2.24 \times 10^{-15}\,\text{C})$; the same

electric charge is used in both PBL and the values are identical to the work of Rahman et al. (2021). A typical concentration (Liu & Dong, 2004) at the bottom of the suspension (top of saltation, $O(1 \text{ m})$) is defined by the baseline concentration of $\mathcal{N}_{baseline} = (n_{b1}, n_{b2}) = (2 \times 10^7 \text{ m}^{-3}, 3.4 \times 10^6 \text{ m}^{-3})$. Four cases are considered in which the virtual wall boundary condition, $\mathcal{N}_w$, is varied from $\mathcal{N}_1 = \mathcal{N}_{baseline}$ (corresponding to a weak storm, and the baseline case) to $40\mathcal{N}_1$ (corresponding to a very strong storm). The term, $\mathcal{N}_w$, represents the concentration of particles at the bottom of the simulation domain (suspension). The cases are labelled as Case I ($\mathcal{N}_w = \mathcal{N}_1 = \mathcal{N}_{baseline}$, 'weak'); Case II ($\mathcal{N}_w = 4\mathcal{N}_1$, 'moderate'); Case III ($\mathcal{N}_w = 10\mathcal{N}_1$, 'strong'); Case IV ($\mathcal{N}_w = 40\mathcal{N}_1$, 'very strong'). The number density is chosen to be non-dimensionalised based on its boundary condition (n_{ws}). Thus, the dimensional number density at any location is given as $\tilde{n}_s n_{ws}$, where $s = 1$ or $s = 2$ in our cases with $\mathcal{N}_w$ as $\mathcal{N}_w = (n_{w1}, n_{w2})$. It is important to note that we characterise the relative storm intensity by uniquely modifying the particle loading and not the characteristics of the PBL flow, as such we maintain the same turbulence intensity, free stream velocity and Reynolds number for all cases on Earth and Mars. The rational is to conduct a more meaningful comparison, while acknowledging that the primary difference among the storms of various strengths lies in the particle-loading and not in the hydrodynamic aspect of the PBL.

Considering the particle of sizes $d_1 = 0.2$ and $d_2 = 0.6$ mm (0.2, 0.5 mm), the density of particles as $\rho_s = 3200$ kg m^{-3} (2650 kg m^{-3}) and viscosity of atmosphere as $\nu = 8.1 \times 10^{-4}$ m^2 s^{-1} (1.48×10^{-5} m^2 s^{-1}). The corresponding particle response time is $\tau_{p1} = 0.55$ and $\tau_{p2} = 4.94$ s (0.32, 2 s). The Stokes number (Crowe, 2005; Loth, 2010) of the particles in such flow is $St_1 = 0.0012$ and $St_2 = 0.01$ (0.005, 0.03) considering (2.1). The corresponding subgrid-scale (SGS) Stokes number (Park, Bassenne, Urzay, & Moin, 2017) of the particles in the LES grid of smallest resolved scale of $\xi/\eta = 1.04 \times 10^4$ (5.86×10^4) is $St_{\xi 1} = 2.6 \times 10^{-6}$ and $St_{\xi 2} = 2.32 \times 10^{-5}$ ($3.2 \times 10^{-6}, 2 \times 10^{-5}$). It is worth noting that Stokes number only accounts for drag effects and does not consider the characteristic electrostatic time scale. However, this modelling approach remains suitable for our selection of the large, bidispersed particles used in the present study because of low Stokes numbers. We selected particles that are sufficiently large to sustain an electric charge and that can be transported via boundary layer turbulence. Although there is a sensitivity to the selection of the particle size, we do not believe that the results would be significantly altered with a different pair of bidispersed particle sizes.

2.3. Physical set-up

To isolate the role of turbulence in charge separation, a canonical turbulent open channel flow is considered to be representative of a PBL. To understand the role of large-scale turbulent motion on the charge separation, LES are run until they reach a statistically steady state. The computational domain is depicted schematically in figure 2. The characteristic dimension of the simulation is taken as the height of the boundary layer, δ. The simulation domain for Mars (Earth) is $x = 32\delta$, $y = 8\delta$ and $z = \delta$, with 640 (768), 192 (192) and 96 (96) grid points in the x, y and z directions, respectively. The simulation domain in the wall-normal direction was truncated and replaced by a virtual wall within the log-layer, in order to model the near-ground particle dynamics. This drastically reduces the computational cost and enables the consideration of the relevant Reynolds number effects. A friction velocity estimate at 0.31 m s^{-1} (0.3 m s^{-1}) gives a friction velocity Reynolds number of $Re_\tau = 2 \times 10^6$ ($Re_\tau = 2 \times 10^7$), table 2. Our choice of a friction velocity ($u_\tau \approx 0.3$ m s^{-1}) in our simulations, while lower than the threshold value (1.5 m s^{-1}) reported by Kok, Parteli, Michaels, and Karam (2012), is motivated by several factors. These factors include the saltation layer not being included in the scope of our study, as well as certain limitations and simplifications inherent to our virtual-wall modelling approach. Furthermore, this friction velocity allowed us to compare a diverse set of solid boundary conditions for Mars and Earth within our framework. The characteristic grid spacing, in viscous wall units, are $\Delta x^+ = 38.4 \times 10^4$ (16×10^5), $\Delta y^+ = 32 \times 10^4$ (16×10^5) and $\Delta z^+ = \xi^+ = 7.7 \times 10^4$ (4×10^5). The virtual wall height ϵ is at $z_\epsilon = 11.25$ m (1.872 m) and in terms of viscous wall units is $z_\epsilon^+ = 1.39 \times 10^4$ (1.5×10^4).
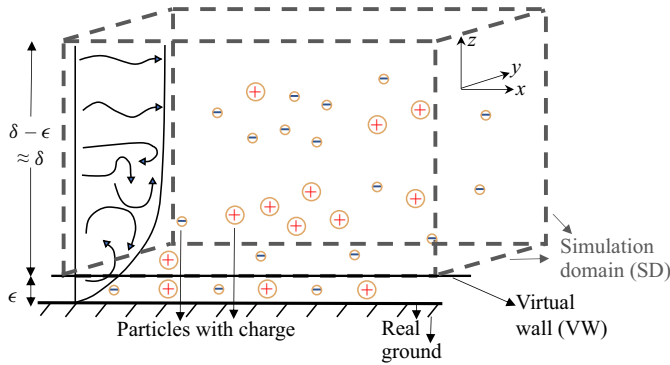
Figure 2. *Schematic of the simulation domain. The virtual wall provides the boundary flux of charged sand particles into the turbulent flow. The atmospheric flow is simulated as an open-channel flow with the lower boundary of the simulation domain being a virtual wall and the domain is doubly periodic.*

Table 2. *Summary of the simulation parameters for charged particle LES of a Martian dust storm.*

Domain size ($L_x/\delta, L_y/\delta, L_z/\delta$)	(32, 8, 1)
Grid size (M_x, M_y, M_z)	(640, 192, 96)
Friction velocity (u_τ)	0.31 m s^{-1}
Friction Reynolds numbers (Re_τ)	2.3×10^6
Grid spacing ($\Delta x^+, \Delta y^+, \Delta z^+$)	($38.4 \times 10^4, 32 \times 10^4, 7.7 \times 10^4$)
Virtual wall height (z_ϵ^+)	1.39×10^4
Resolved scale ($\xi^+, \xi/\eta, \delta/\xi$)	($7.7 \times 10^4, 1.04 \times 10^4, 96$)

2.4. Governing equations

This work uses the same LES framework described in Rahman et al. (2021), which solves the filtered incompressible Navier–Stokes equations in the continuum phase along with an Eulerian particle transport equation with DQMOM. The equations are non-dimensionalised by the free stream velocity ($U_f = U_\infty$) and the boundary layer thickness ($L_f = \delta$). The generic equations for the fluid motion are

$$\frac{\partial \tilde{u}_i}{\partial x_i} = 0, \tag{2.2}$$

$$\frac{\partial \tilde{u}_i}{\partial t} + \frac{\partial \tilde{u}_i \tilde{u}_j}{\partial x_j} = \frac{1}{Re} \frac{\partial^2 \tilde{u}_i}{\partial x_j^2} - \frac{\partial \tilde{p}}{\partial x_i} - \frac{\partial T_{ij}}{\partial x_j} + f(t)\delta_{i1}, \tag{2.3}$$

where $\tilde{u}_i$ is the filtered non-dimensional fluid velocity, $\tilde{p}$ is the non-dimensional pressure and $T_{ij} = \widetilde{uu} - \tilde{u}\tilde{u}$ is the subgrid stress tensor. The LES employs stretched spiral vortex SGS model and a virtual wall model similar to the previous work by Rahman and Samtaney (2017). A source term, $f(t)$, corresponds to a time-varying body force throughout the domain which maintains a constant mass flow in streamwise direction.

Note that we neglected the gravitational acceleration in this study despite the large particle size. Although this deliberate choice could affect the final distribution of the particles, we opted to make this assumption to focus uniquely on the turbulence-driven nature of the charge separation in the PBLs. In order to assess the relative importance of the gravitational force, we can define the magnitude of the Kolmogorov acceleration as $a_k = \epsilon^{2/3}/\eta^{1/3}$, where the dissipation rate is tied to $\epsilon \approx U^3/L$ and the Kolmogorov length scale is approximately: $\eta \approx L/Re^{3/4}$. If we consider the free stream velocity and boundary layer height as the characteristic velocity and length scale, we can estimate

the Kolmogorov acceleration. Generally it is accepted that if the Kolmogorov acceleration is large relative to the gravitational acceleration, the flow is turbulence dominated and gravitational effects can be neglected. On Earth, gravity can reasonably be neglected ($a_k = 40.3$ m s^{-2}, $g = 9.81$ m s^{-2}) as done in Rahman et al. (2021); on Mars, this assumption breaks down ($a_k = 3.04$ m s^{-2}, $g = 3.72$ m s^{-2}) and gravitational settling should not, in a representative case, be neglected. To maintain our focus on turbulence-driven charge separation in the boundary layer, we opted to neglect the gravitational contribution in both the terrestrial and Martian PBLs. This assumption is further justified by the fact that in a realistic Martian PBL, gravitational settling would be counterbalanced by other forces such as buoyant thermal convection in the atmosphere (Spiga, 2021; Wu et al., 2021), which we have not modelled to maintain a reasonable comparison of both PBLs.

The Eulerian form of the particle phase conservation equations, shown in (2.4) and (2.7), are similarly non-dimensionalised. We assume that all particle collisions and resulting triboelectric charging, occurs near the wall, hence these effects are modelled as part of the virtual wall. Outside the virtual wall, in other words, inside our computational domain, we consider the particles to be collisionless. The particle transport equation includes the electrostatic Poisson equation in addition to the one-way momentum exchange. The equation set for the particle transport in an Eulerian framework is

$$\frac{\partial \tilde{v}_{Si}}{\partial t} + \tilde{v}_{Sj} \frac{\partial \tilde{v}_{Si}}{\partial x_j} = \tilde{\mathcal{D}}_{Si} + \epsilon_{Si}, \tag{2.4}$$

$$\tilde{\mathcal{D}}_{Si} = \frac{\rho_f}{\rho_s} \frac{18 \nu L_f}{d_s^2 U_f} \left(1 + 0.15 Re_S^{0.687}\right) (\tilde{u}_i - \tilde{v}_{Si}), \tag{2.5}$$

$$\epsilon_{Si} = \frac{\partial \Phi_S}{\partial x_i}, \quad \frac{\partial^2 \Phi_S}{\partial x_i^2} = -\frac{L_f^2}{U_f^2} \frac{\sigma_s}{\rho_s} \frac{\Sigma}{\varepsilon}, \quad \Sigma = \sum_{s=1}^{s=s_n} n_{ws} \tilde{n}_S q_s, \tag{2.6a–c}$$

$$\frac{\partial \tilde{n}_S}{\partial t} + \frac{\partial (\tilde{n}_S \tilde{v}_{Si})}{\partial x_i} = 0. \tag{2.7}$$

Here, $\tilde{v}_{Si}$ corresponds to the average particle velocity of species s. Also, σ_s is the dimensional charge density ($\sigma_s = q_s/(\pi d_s^3/6) = q_s \rho_s / m_s$) of the particles species s. Here, $\tilde{\mathcal{D}}_S$, ϵ_S and Φ_S represent the drag force term (Stokes drag), the electrostatic force term and the electric potential of particles, respectively. The drag force is a momentum exchange term in the particle equation that accounts for the one-way coupling from the atmospheric flow. The Reynolds number of the particle is defined as $Re_S = |\tilde{u} - \tilde{v}_S| U_f d_s / \nu$. The dimensional electric field at any location is given as

$$E_i = -\rho_s U_f^2 \, \epsilon_{Si} \, /(\sigma_s L_f). \tag{2.8}$$

The dimensionless electric potential is defined from its non-dimensional parameter as

$$\phi = U_f^2 \Phi_S \rho_s / \sigma_s. \tag{2.9}$$

The above governing equations are implemented in the solver and computed throughout the computational domain.

2.5. Numerical methods

We adopt the numerical algorithms based on a staggered grid with the pressure and number density of the particles located at the cell centre. The velocity components ($\tilde{u}_i$ and $\tilde{v}_{Si}$) are defined at the face centres of the mesh in the usual manner. For the particle phase, the DQMOM is chosen in which the weights and abscissas of the quadrature approximation are tracked directly rather than the moments themselves. The numerical method in this framework is based on a fractional-step algorithm with an energy-conservative,

fourth-order finite-difference scheme on a staggered mesh; the skew-symmetric form of spatial discretisation is used to minimise the aliasing errors. We adopt the third-order Runge–Kutta time integration to advance the governing equations. We can classify the fluid equations into linear and nonlinear operators, as done in Spalart, Moser, and Rogers (1991). Further, following the LU decomposition notation of Perot (1993), we arrive at the intermediate velocity Helmholtz equation, pressure Poisson equation and velocity correction equation. Similarly, for the particle phase, third-order accuracy can be achieved by using three substeps in the time advancement.

3. Results

3.1. *Characteristics of the turbulent flow*

Prior to simulating flows with the charged, particle-laden motion, we first evaluate the SGS model in a WMLES context. We recall that we model the atmospheric boundary layer as an open channel flow at very high-Reynolds number. Both the SGS and the WMLES contribute to enabling a representative PBL at these large Reynolds number. The use of open-channel flows as a representative PBL either as a direct numerical simulation (DNS) (e.g. Atoufi, Scott, & Waite, 2019) or as very large-eddy simulations (Aliabadi, Veriotes, & Pedro, 2018) have been reported in the literature. Here, we verify the use of the stretched vortex SGS model and the associated wall-model (see Chung & Pullin, 2009) for high Reynolds number turbulent channel flow in our simulation framework. The single-phase channel flow is run at a Reynolds number of $Re = 10^9$ with a friction Reynolds number of $Re_\tau = 20 \times 10^6$, as shown in figure 3. The extensive log-region is compared with the analytical law-of-the-wall and DNS data of Hoyas and Jiménez (2006), noting that we are comparing an open channel flow with a turbulent channel flow. The departure from the log-law, and especially the inward arc of the profile, is attributable to the Neumann boundary condition used at the top boundary; similar velocity profiles are seen in other open-channel flow simulations (Aliabadi et al., 2018; Atoufi et al., 2019). The validation of turbulence distribution for the simulations are in figure 3(*b*). Additional validation of the solver can be found in Rahman (2020) and the validation with experimental observation of the electric field in terrestrial sandstorms was undertaken by Rahman et al. (2021).

3.2. *Particle concentration distribution*

The comparative analysis of the Martian and terrestrial results is first undertaken for Case III, which corresponds to a strong storm condition. Later, in § 3.4, the results of all cases are aggregated and compared.

There is a significant difference in the distribution of the mean particle number density between the Martian and terrestrial PBL, despite the identical particle concentration imposed near the wall. In figure 4(*a*,*b*), we plot the wall-normal variation (z/δ) of the mean normalised particle number density for both the small ($\overline{n}_1$) and large particles ($\overline{n}_2$). These quantities are averaged along the streamwise and spanwise directions as well as over time during the statistically quasisteady-state regime. We note that the mean concentration profile for the number density is significantly lower on Mars than on Earth, especially approaching the virtual wall. The difference is primarily attributable to the rarefied Martian atmosphere, and more specifically to the much lower density, which leads to a lower particle drag force, and therefore impedes the momentum transfer from the fluid to the particles necessary for their transport. We observe that the mean concentration of both the small (negatively charged) and large (positively charged) particles on Mars, slightly increases with distance from the virtual wall. This contrasts with the behaviour on Earth for which we get a monotonic decrease of particle density as we move away from the wall. The density is approximately two orders of magnitude smaller on Mars, concomitantly, the drag force on the particles is reduced by a similar magnitude, hence the electrostatic force (which is maximum at the virtual wall) plays a relatively larger role on Mars compared with Earth.
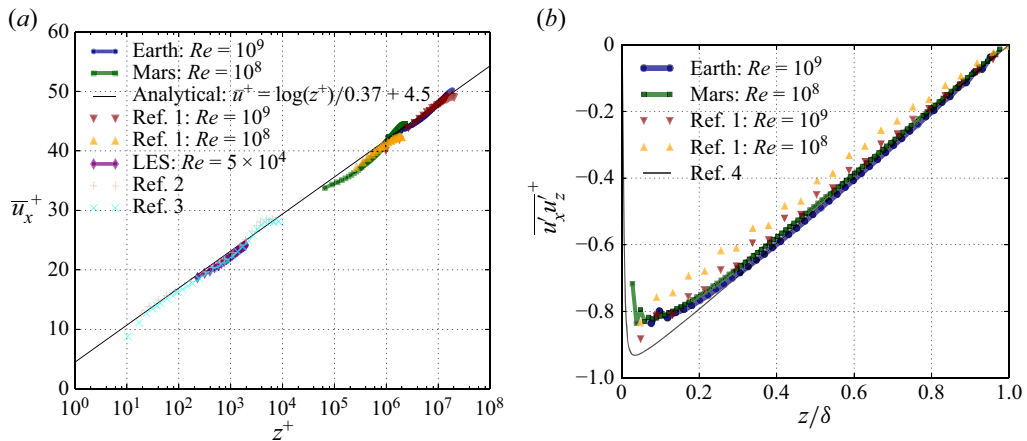
Figure 3. *Simulated LES channel cases of (a) normalised streamwise velocity ($\bar{u}_x^+$) with normalised height (z^+) and their comparison with analytical model and data of Chung and Pullin (2009) (Ref. 1), Fernholz and Finleyt (1996) (Ref. 2), Krogstad and Efros (2012) (Ref. 3), and (b) variation of normalised streamwise wall-normal fluctuations with normalised height. The normalised wall-normal fluctuations are reproduced from the DNSs of Hoyas and Jiménez (2006) (Ref. 4) where $Re_\tau = 2 \times 10^3$.*

Similarly, in figure 4(c,d), we observe that the root mean square (r.m.s.) of the smaller-sized particle concentration is an order of magnitude lower than those of the larger particles, which is similar on both planets. This is tied to the difference in the aerodynamic Stokes number of the small and large particles, which is defined as the ratio of the time scale of the particles and the flow; similar to the observation in Di Renzo and Urzay (2018). The greater relative importance of the electrostatic force is driving the greater particle density variability in the outer parts of the boundary layer, whereas on Earth, these are primarily driven by the hydrodynamic effects. It is worth noting that the r.m.s. fluctuations of the number density in figure 4(c,d) tend towards zero with a similar slope at the outer part of the boundary layer. The electrostatic forces are minimal but the hydrodynamic drag remain non-negligible in the outer parts of the log-layer.

3.3. Charge density and electric fields

The mean charge density shown in figure 5(a) is related to the differentially charged particle distribution discussed in the previous subsection (recall figure 4) and is defined as $\overline{\Sigma} = n_{w1}\bar{n}_1 q_1 + n_{w2}\bar{n}_2 q_2$. When we dimensionalise the particle number density near the virtual wall in figure 4(a,b), we observed roughly the same particle number densities for both the small and large particles on Mars. As the smaller particles carry a greater (in magnitude) negative charge compared with the positive charge of the larger particles, we have negative mean charge density just above the virtual wall. Overall, this is the result of the turbulent transport of different sized particles and large-scale charge separation at different altitudes. On Earth, the mean charge density remains positive through the boundary and is maximum near the virtual wall due to the greater number density of larger particles. We remind the reader that neither gravitational settling nor buoyant updrafts are considered in the present simulation to focus primarily on the turbulent-transport aspect of the charge separation.

Despite the differences in the mean charge density, the mean electric potential consistently increases with altitude on Earth and Mars, as shown in figure 5(b). The mean electric potential remains positive with altitude because of the corresponding domain charge density variation. The rate of increase of electric potential in the vertical direction represents the strength of the wall-normal electric field. The mean electric field due to the turbulence-induced charge separation is depicted in figure 5(c). The wall-normal component of the electric field remains negative throughout the boundary layer, with the
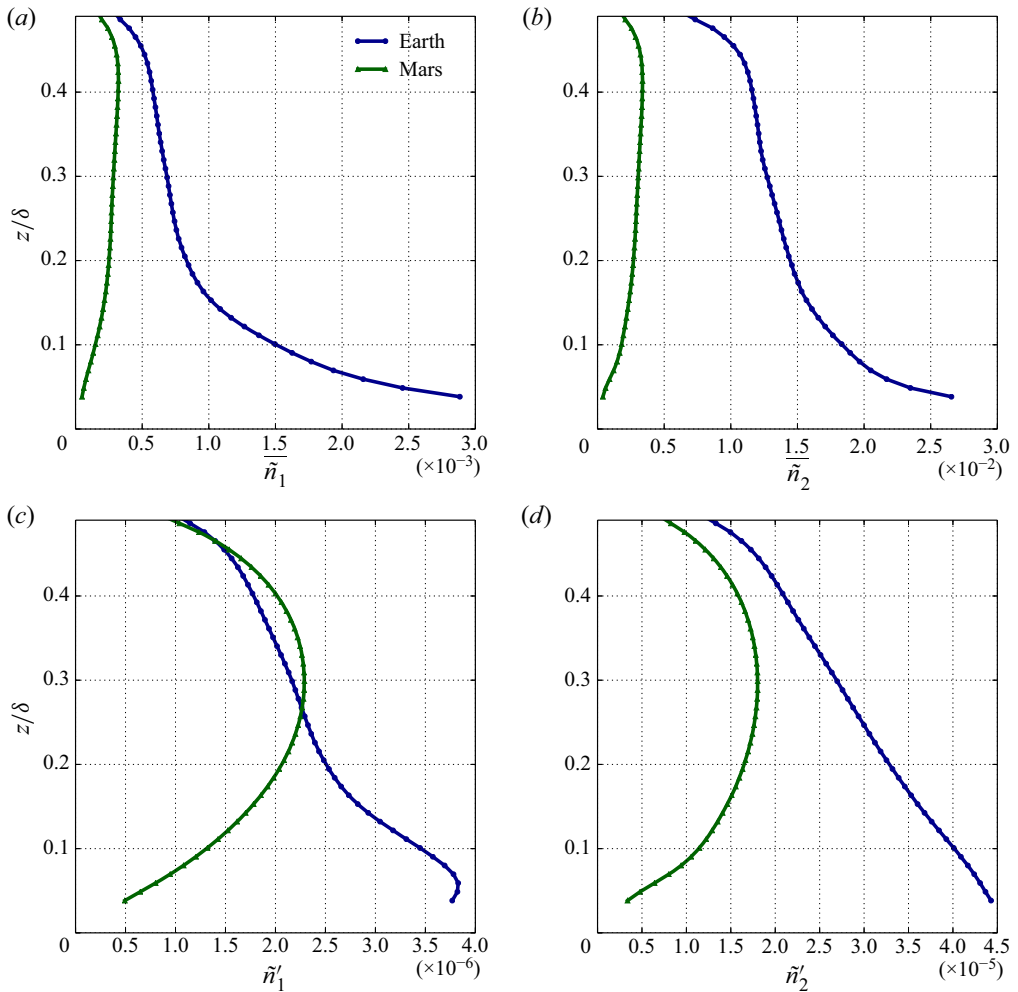
Figure 4. *Normalised charged particle concentration (a,b) and r.m.s. concentration (c,d) in the wall-normal direction for Case III $(n_{w1}, n_{w2}) = 10(n_{b1}, n_{b2}) = (2 \times 10^8, 3.4 \times 10^7 \text{ m}^{-3})$. The left-hand column corresponds to the small size particles (s = 1) and right-hand column the large size particles (s = 2).*

terrestrial electric field being over an order of magnitude stronger than on Mars, for the same near-wall particle concentration. This means that the direction of the wall-normal electric field is vertically downward based on the negative gradient of the electric potential. The mean total electric field (i.e. the magnitude of the electric field vector), shown in figure 5(*d*), decreases with height, as expected. The qualitative similarities with figure 5(*c*) implies that the mean electric fields in the horizontal (streamwise/spanwise) directions are negligible in comparison with the mean wall-normal electric field. Indeed, the mean spanwise electric field magnitude is of the order of machine precision, while the mean streamwise electric field magnitude is slightly higher than the machine precision (but still negligible in comparison with the mean wall-normal electric field). This slightly higher magnitude in the streamwise direction is mainly due to the quasiparallel flow assumption, which is necessary for the streamwise periodicity of the open channel simulations.

The order-of-magnitude lower electric field on Mars compared with Earth aligns with the findings of Melnik and Parrot (1998) who found a slightly higher maximum electric field (1–2 kV m^{-1}). Other
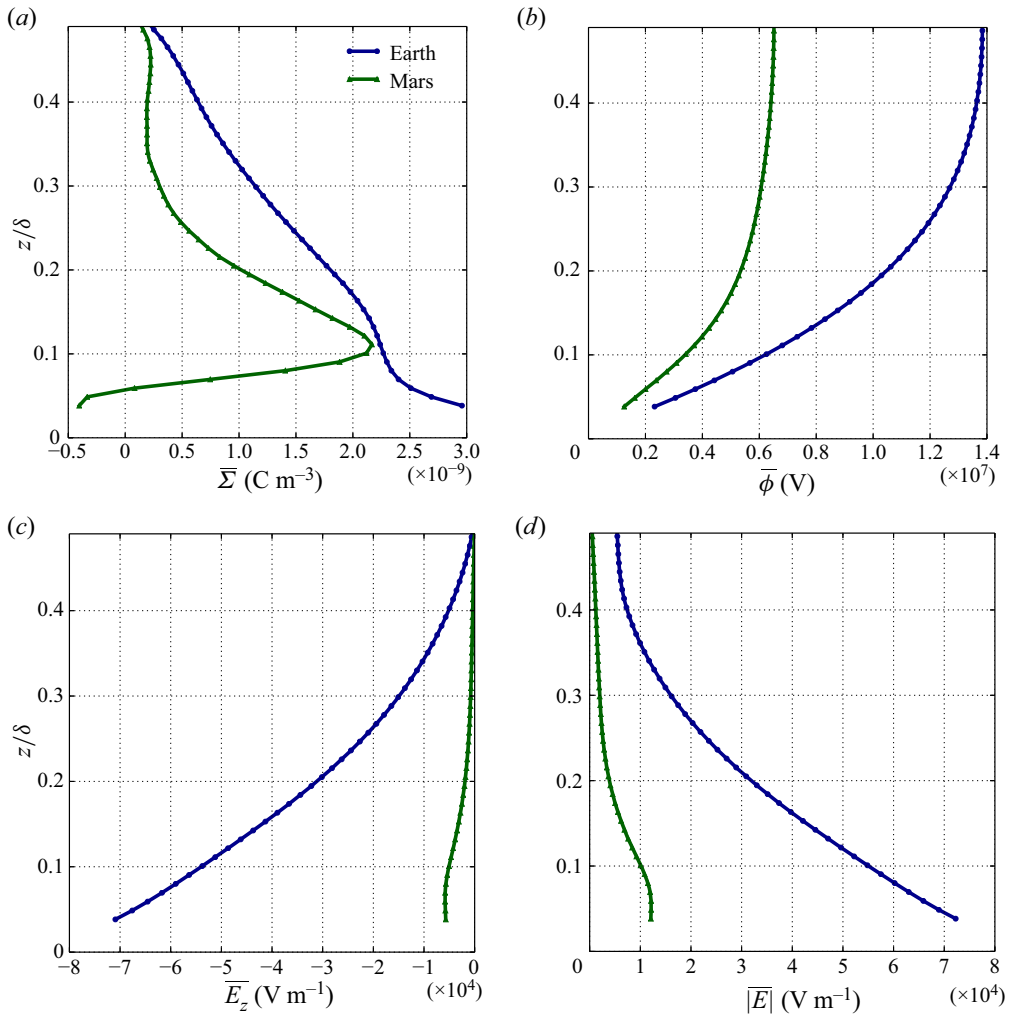
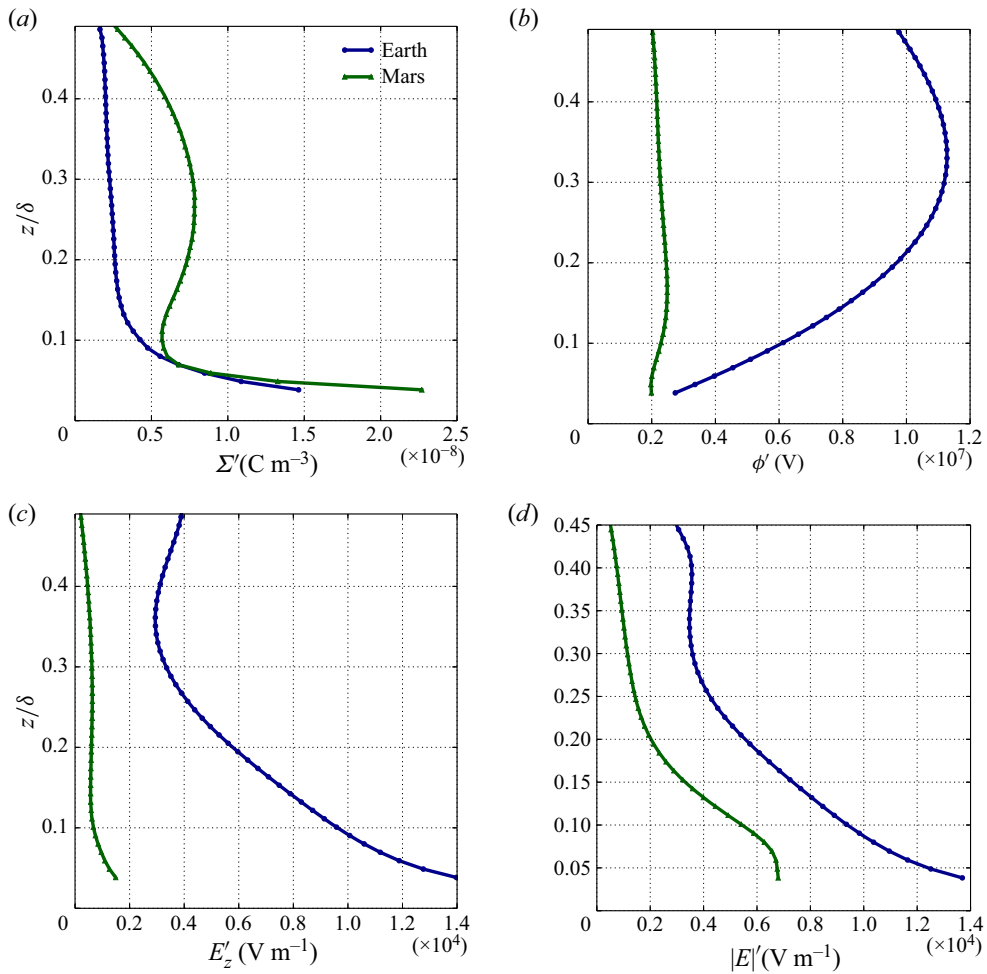**Figure 5.** *Mean altitude variation of (a) charge density, $\bar{\Sigma}$ (C m^{-3}), (b) electrostatic potential, $\bar{\phi}$ (V), (c) wall-normal electric field, $\bar{E}_z$ (V m^{-1}) and (d) net electric field, $|\bar{E}|$ (V m^{-1}) for Case III.*

works, such as Farrell, Delory, Cummer, and Marshall (2003), found that Martian dust devils could develop charge separations of up to 20 kV m^{-1}.

The r.m.s. of the charge density, shown in figure 6(*a*), increases rapidly on both Earth and Mars as we approach the ground (below $z/\delta < 0.1$). This can be attributed to the high turbulence intensity near the wall, as stated earlier. Figure 6(*b*) shows very different behaviour of electric potential r.m.s. in the two PBLs. On Mars, ϕ' does not show much dependence on altitude with a small peak r.m.s. at around $z/\delta = 0.15$, while it rises steeply on Earth with the peak fluctuations arising much farther away from the wall. Figure 6(*c*) depicts the fluctuation characteristics of the wall-normal electric field (E_z') and figure 6(*d*) shows the r.m.s. of electric field magnitude.

### 3.4. Effect of storm strength on electric field

The aggregated results for all storm conditions, on both Earth and Mars, are summarised in figures 7 and 8. For the terrestrial sandstorm, the results are compared with field measurements (denoted by the symbols near the ground). In figure 7, the marks are average and r.m.s. magnitudes measured from

Figure 6. *Altitude based variation in the fluctuations of (a) charge density, Σ' (C m^{-3}), (b) electric potential, ϕ' (V), (c) wall-normal electric field E_z' (V m^{-1}) and (d) net electric field $|E|'$ (V m^{-1}).*

different terrestrial sandstorm data of Zhang et al. (2004) (circles) and Zhang et al. (2018) (stars). On Mars, the mean electric field and its fluctuations never reach the strength of a sandstorm on Earth; even for the most severe Martian storms. This lower strength of the Martian electric field is because of its smaller magnitude of Martian atmospheric Reynolds number, the corresponding lower level of turbulence, and lower density and viscosity. Further, Mars has a much lower threshold electric field of 25 kV m^{-1}, which will cause localised electrical discharges before it can reach higher electric field magnitudes, and lightning, as observed on Earth. One key observation is the strong self-similarity in the electric field profiles for lower storm intensities on both Earth and Mars. This implies that we can expect mostly monotonic behaviour with the lower storm strength, assuming the ratio of small-to-large particles remains unchanged at different storm conditions. We do note that the electric field on Mars (figure 8a) seems to reach a self-regulating state in which the electric field does not increase with storm strength. We note that Cases II, III and IV display similar electric field profiles. This self-regulating state appears to be reached on Earth at higher storm intensity with higher electric field intensity. It is hypothesised that this self-regulation arises due to the greater relative importance of the electric potential in transporting particles on Mars, compared with the viscous drag force. A somewhat analogous self-regulating behaviour was noted in Di Renzo and Urzay (2018) for differentially charged
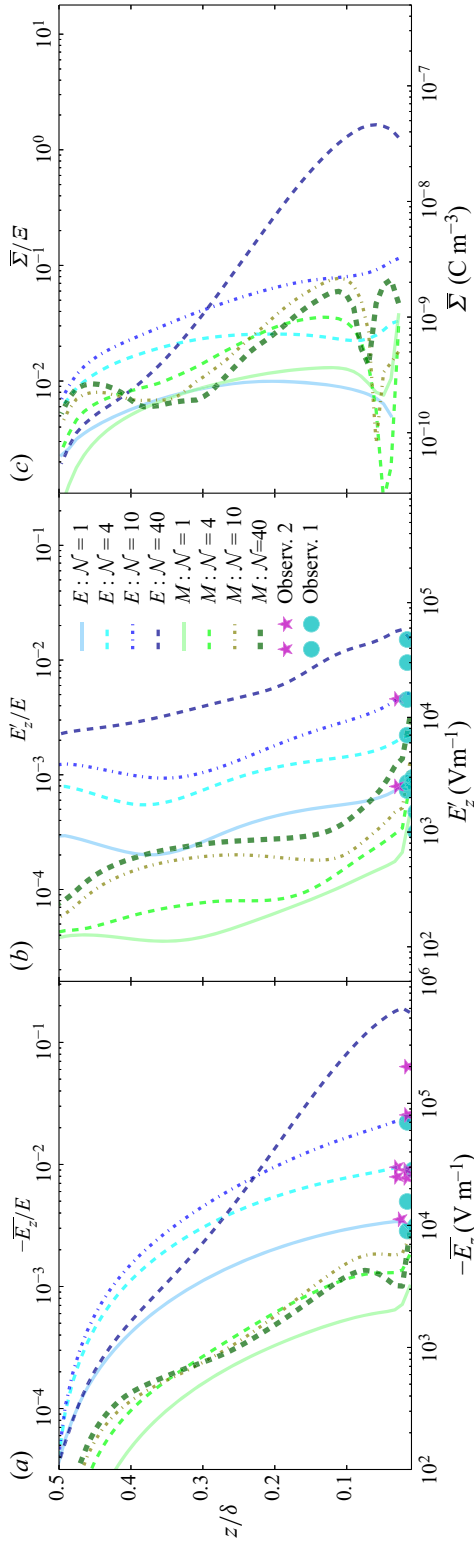
Figure 7. *Wall-normal height variation of the vertical electric field (a) average (spanwise/streamwise and time mean) of $\bar{E}_z$, (b) the r.m.s. fluctuations of E_z' and (c) average charge density, where $\mathcal{E} = \delta\Xi/\varepsilon$ and $\Xi = s_n M(n_{b1}|q_1|, n_{b2}|q_2|)$ are, respectively, the reference electric field and charge density values corresponding to Case 1 (M(a, b) = average of a and b). The symbols are mean and r.m.s. values synthesised from various terrestrial sandstorm measurements by Zhang, Wang, Qu, and Yan (2004) (circles, Observ. 1) and Zhang, Li, and Bo (2018) (stars, Observ. 2).*
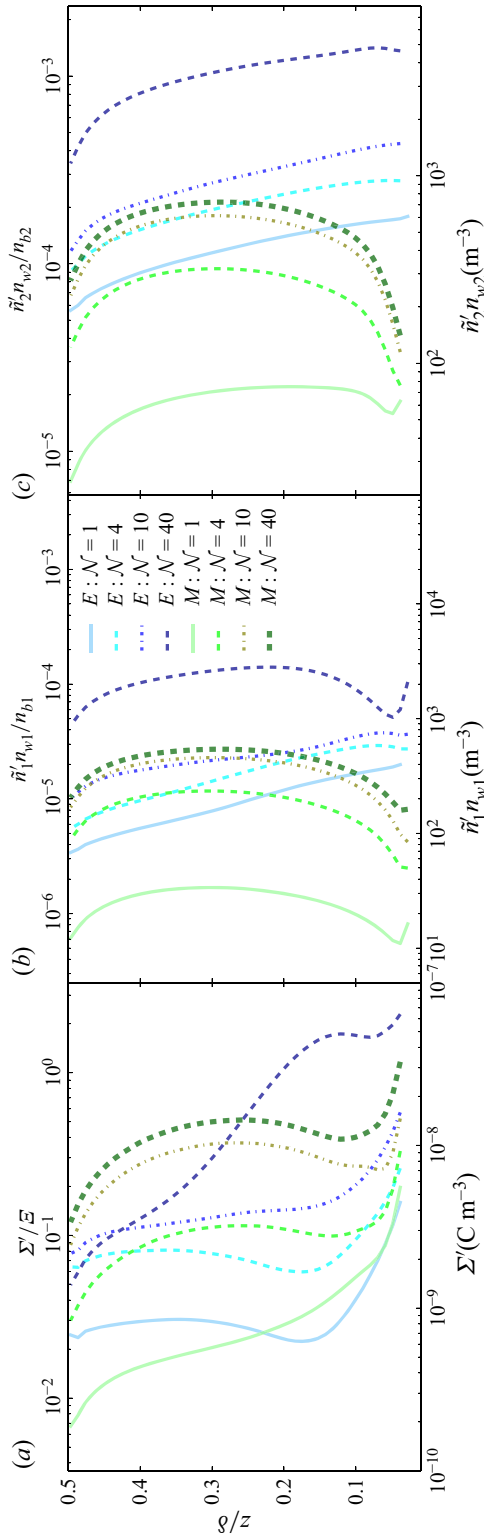
Figure 8. *Wall-normal height-based variation in the (a) charge density fluctuations, (b) normalised r.m.s. concentration of the charged small and (c) large particles.*
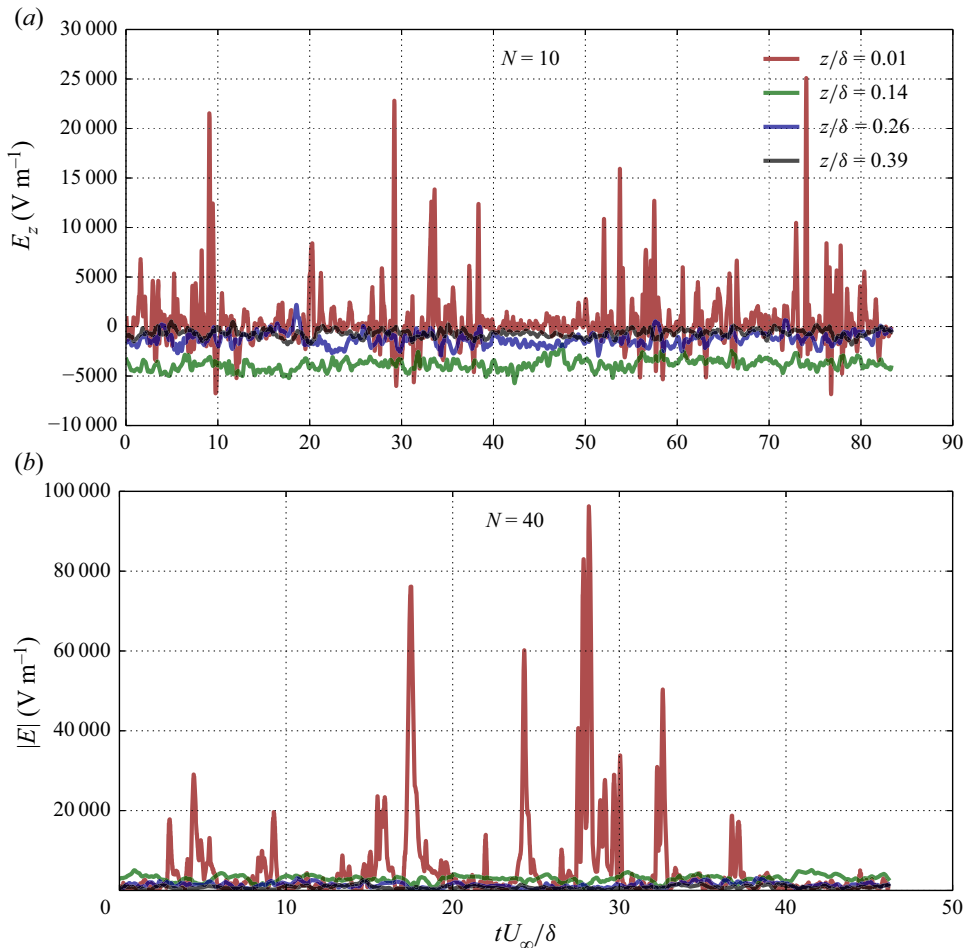
Figure 9. *Time variation of the (a) wall normal electric field of $N = 10$ (Case III) and (b) absolute electric field of $N = 40$ (Case IV).*

particles in isotropic turbulence. The charge separation is driven by viscous transport via the difference in aerodynamic Stokes number of the small and large particles. On Mars, the electrostatic force component is relatively more important than on Earth. This is due to the lower drag on Mars than on Earth, from (2.5), assuming the occurrence of the same charge distribution. The electrostatic force acts to reduce the electric field magnitude, but the dominating drag force on Martian particles reduces this electrostatic drive causing higher electric fields. As the electric field gets stronger, so does the impact of the electric field on the particle transport, further impeding the charge separation caused by viscous drag effects resulting in a self-limiting behaviour of the electric field.

### 3.5. Temporal variation in electric field

Although, time-averaged statistical data provides information on the turbulence-driven charge separation, the temporal variation of the electric field is necessary to understand the probability of a local electric discharge event, which occurs in the form of sparks or lightning. We note that our simulations do not explicitly model the discharge events, nor do we modify the particle charges after such an event. Nonetheless, we define the threshold value, based on the literature, from which we would expect a
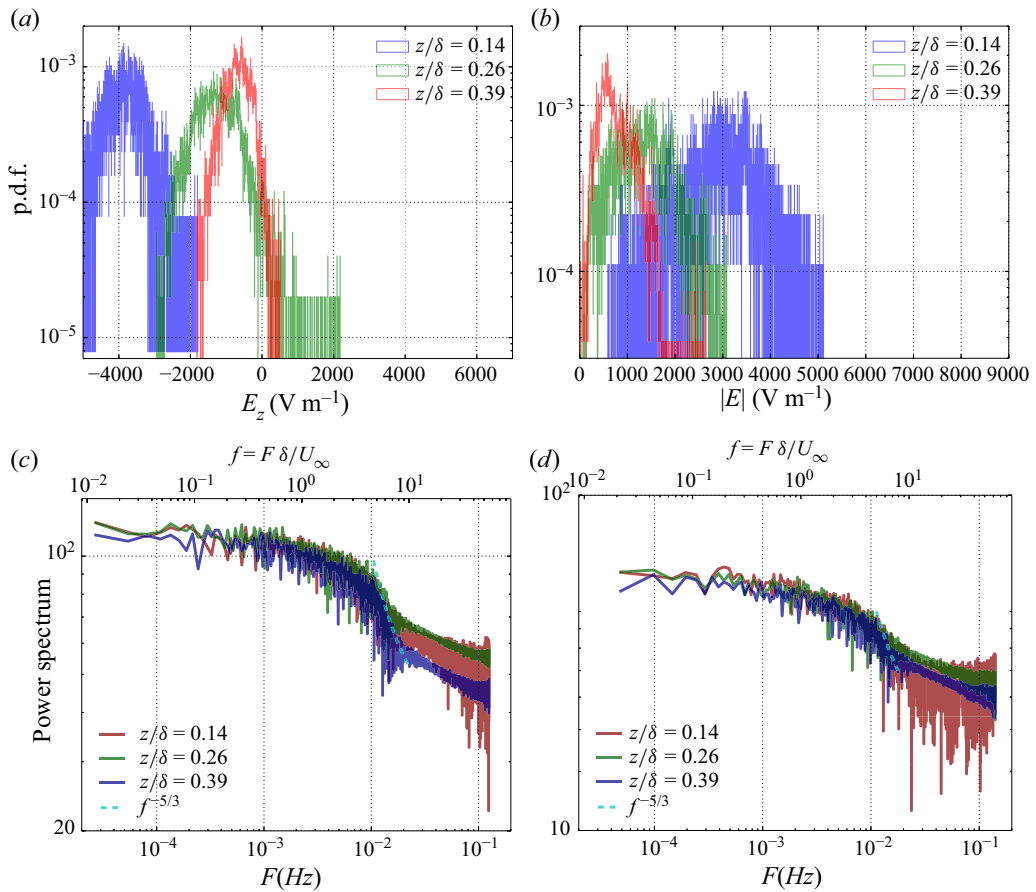
Figure 10. *The probability density distribution for (a) $\mathcal{N} = 10$ of wall-normal electric field (E_z) and for (b) $\mathcal{N} = 40$ of absolute electric field ($|E|$) along with the corresponding power spectrum of (c) $\mathcal{N} = 10$ and (d) $\mathcal{N} = 40$. These power spectrum plots of electric fields are compared with the $-5/3$ power law, $f^{-5/3} \sim F^{-5/3}$, within intermediate scales. p.d.f., probability density function.*

discharge event to occur. The comparative temporal variation of the electric field for the terrestrial simulations has been reported in Rahman et al. (2021).

We plot the time variation of E_z at various wall-normal locations in figure 9(*a*) for the strong (Case III) and figure 9(*b*) very strong (Case IV) Martian dust storms. As the turbulent flow field is statistically steady, the selection of time, $t = 0$, is therefore somewhat arbitrary once the initial transient of the simulation is complete. In both the weak and strong dust storms, we note distinctive and very compact peaks in the electric field that occur primarily near the wall. Unsurprisingly, the magnitudes of the peaks are much larger for the strong storms and roughly scale with the increased near-wall particle concentration. The probability density distribution and power spectrum of the electric field, in figure 10, show a similar and broad distribution of these electric peaks, which highlights the stochastic nature that is modulated by the turbulent flow field. Upon meticulous examination of our data, we observe that our electrohydrodynamic power spectrum exhibits a scaling behaviour consistent with the Kolmogorov $-5/3$ power law within the intermediate scales of frequency. This observation is consistent with the recent field measurements of dust storms on Earth as cited in Zhang and Zhou (2023), and it underscores the relevance and significance of our findings. This similarity between the electric field dynamics in our dust storms and other studied systems underscores the potential universality of this scaling behaviour. These peaks in the electric field may overcome the breakdown voltage of the Martian atmosphere,
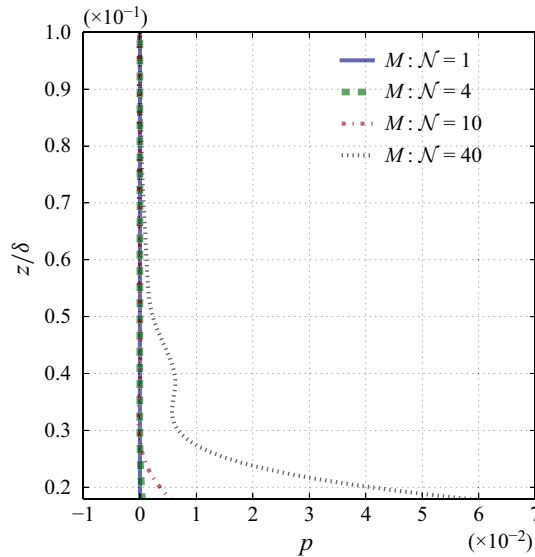
Figure 11. *Altitude variation of probability function crossing the threshold electric field.*

which results in discharge events. To quantify the probability of electrical discharge events at various wall-normal locations, we define the probability, integrated in both time and space, as

$$p(z) = \frac{1}{T}\frac{1}{L_x}\frac{1}{L_y} \int_{t=0}^{T} \int_{0}^{L_y} \int_{0}^{L_x} P(x, y, z, t)\, \mathrm{d}x\, \mathrm{d}y\, \mathrm{d}t, \qquad (3.1)$$

where

$$P(x, y, z, t) = \begin{cases} 1 & \text{if } |E| \geq E_T, \\ 0 & \text{if } |E| < E_T. \end{cases} \qquad (3.2)$$

Here E_T is the breakdown voltage on Mars defined in table 1. Therefore, $p(z)$ provides a statistical measure of the likelihood of occurrence at a given altitude z. Figure 11 shows the probability of a breakdown event. As observed in the time evolution plot, the highest probability occurs near the wall and we observe that the significant probability of discharge events occurs in the strongest Martian storm (Case IV). The maximum probability is as high as 6 %, thus discharge events remain significantly more frequent than on Earth. For Case III, the probability is as high as 1 %. There is still a probability of discharge event for the other weaker cases.

4. Conclusions

This work uses wall-modelled LES to explore the differences in the turbulence-induced charge separation in particle-laden planetary boundary layer flows on Earth and Mars. In particular, we seek to understand the physical reasons that could explain the infrequent lightning observations on Mars, despite the much lower electric breakdown potential of its atmosphere. To this end, high Reynolds number, open channel flows, selected as a representative planetary boundary layers are simulated under Martian and terrestrial conditions. There are two main reasons to explain the less frequent occurrence of lightning on Mars. Firstly, the rarefied atmosphere impedes the particle transport, resulting in a much weaker electric field generations. Secondly, we note discharge events occur very close to the ground and are very significant in the most severe dust storms (Cases III and IV). The equivalent terrestrial sandstorm has much higher breakdown potential, greater by approximately two orders of magnitude. In a 'moderate' dust storm on

Mars, we do not expect to observe any significant large-scale lightning, which help elucidate previous experimental observations but we may still observe localised electric discharge events. We note a self-limiting state in the charge separation on Mars which is attributable to the weaker importance of the viscous particle transport.

References

Aliabadi, A.A., Veriotes, N., & Pedro, G. (2018). A very large-eddy simulation (VLES) model for the investigation of the neutral atmospheric boundary layer. *Journal of Wind Engineering and Industrial Aerodynamics*, *183*, 152–171.

Anderson, M.M., Siemion, A.P.V., Barott, W.C., Bower, G.C., Delory, G.T., De Pater, I., & Werthimer, D. (2011). The allen telescope array search for electrostatic discharges on Mars. *The Astrophysical Journal*, *744*(1), 15.

Atoufi, A., Scott, K.A., & Waite, M.L. (2019). Wall turbulence response to surface cooling and formation of strongly stable stratified boundary layers. *Physics of Fluids*, *31*(8), 085114.

Balachandar, S., & Eaton, J.K. (2010). Turbulent dispersed multiphase flow. *Annual Review of Fluid Mechanics*, *42*, 111–133.

Banfield, D., Spiga, A., Newman, C., Forget, F., Lemmon, M., Lorenz, R., . . . Banerdt, W.B. (2020). The atmosphere of Mars as observed by InSight. *Nature Geoscience*, *13*(3), 190–198.

Bertrand, T., Wilson, R.J., Kahre, M.A., Urata, R., & Kling, A. (2020). Simulation of the 2018 global dust storm on Mars using the NASA Ames Mars GCM: A multitracer approach. *Journal of Geophysical Research: Planets*, *125*(7), e2019JE006122.

Burr, D.M., Sutton, S.L.F., Emery, J.P., Nield, E.V., Kok, J.F., Smith, J.K., & Bridges, N.T. (2020). A wind tunnel study of the effect of intermediate density ratio on saltation threshold. *Aeolian Research*, *45*, 100601.

Calaf, M., Meneveau, C., & Meyers, J. (2010). Large eddy simulation study of fully developed wind-turbine array boundary layers. *Physics of Fluids*, *22*(1), 015110.

Chen, W., Lovejoy, S., & Muller, J.P. (2016). Mars' atmosphere: The sister planet, our statistical twin. *Journal of Geophysical Research*, *121*(20), 11968–11988.

Chung, D., & Pullin, D.I. (2009). Large-eddy simulation and wall modelling of turbulent channel flow. *Journal of Fluid Mechanics*, *631*, 281–309.

Cimarelli, C., Alatorre-Ibargüengoitia, M.A., Kueppers, U., Scheu, B., & Dingwell, D.B. (2014). Experimental generation of volcanic lightning. *Geology*, *42*(1), 79–82.

Crowe, C.T. (2005). *Multiphase flow handbook*. Boca Raton, FL: CRC Press.

Crowe, C.T., Gore, R.A., & Troutt, T.R. (1985). Particle dispersion by coherent structures in free shear flows. *Particulate Science and Technology*, *3*(3–4), 149–158.

Di Renzo, M., & Urzay, J. (2018). Aerodynamic generation of electric fields in turbulence laden with charged inertial particles. *Nature Communications*, *9*(1), 1–11.

Duff, N., & Lacks, D.J. (2008). Particle dynamics simulations of triboelectric charging in granular insulator systems. *Journal of Electrostatics*, *66*(1–2), 51–57.

Farrell, W.M., Delory, G.T., Cummer, S.A., & Marshall, J.R. (2003). A simple electrodynamic model of a dust devil. *Geophysical Research Letters*, *30*(20), 1–4.

Fernholz, H.H., & Finleyt, P.J. (1996). The incompressible zero-pressure-gradient turbulent boundary layer: An assessment of the data. *Progress in Aerospace Sciences*, *32*(4), 245–311.

Forward, K.M., Lacks, D.J., & Sankaran, R.M. (2009). Particle-size dependent bipolar charging of Martian regolith simulant. *Geophysical Research Letters*, *36*(13), L13201. https://agupubs.onlinelibrary.wiley.com/doi/pdf/10.1029/2009GL038589.

Haberle, R.M., Clancy, R.T., Forget, F., Smith, M.D., & Zurek, R.W. (2017). *The atmosphere and climate of Mars*. Cambridge, UK: Cambridge University Press.

Harper, J.M., Dufek, J., & McDonald, G.D. (2021). Detection of spark discharges in an agitated Mars dust simulant isolated from foreign surfaces. *Icarus*, *357*, 114268.

Hoyas, S., & Jiménez, J. (2006). Scaling of the velocity fluctuations in turbulent channels up to re τ = 2003. *Physics of Fluids*, *18*(1), 011702.

Izvekova, Y.N., & Popel, S.I. (2017). Plasma effects in dust devils near the Martian surface. *Plasma Physics Reports*, *43*(12), 1172–1178.

Izvekova, Y.N., Popel, S.I., & Izvekov, O.Y. (2022). Dust and dusty plasma effects in Schumann resonances on Mars: Comparison with Earth. *Icarus*, *371*, 114717.

Jackson, T.L., & Farrell, W.M. (2006). Electrostatic fields in dust devils: An analog to Mars. *IEEE Transactions on Geoscience and Remote Sensing*, *44*(10), 2942–2949.

Kaimal, J.C., & Finnigan, J.J. (1994). *Atmospheric boundary layer flows: Their structure and measurement*. New York, NY: Oxford University Press.

Kok, J.F., Parteli, E.J.R., Michaels, T.I., & Karam, D.B. (2012). The physics of wind-blown sand and dust. *Reports on Progress in Physics*, *75*(10), 106901.

Kok, J.F., & Renno, N.O. (2006). Enhancement of the emission of mineral dust aerosols by electric forces. *Geophysical Research Letters*, *33*(19), 2–6.

Kok, J.F., & Renno, N.O. (2008). Electrostatics in wind-blown sand. *Physical Review Letters*, *100*(1), 014501.

Kok, J.F., & Renno, N.O. (2009). Electrification of wind-blown sand on Mars and its implications for atmospheric chemistry. *Geophysical Research Letters*, *36*(5), L05202.

Krogstad, P.-Å., & Efros, V. (2012). About turbulence statistics in the outer part of a boundary layer developing over two-dimensional surface roughness. *Physics of Fluids*, *24*(7), 075112.

Kruss, M., Salzmann, T., Parteli, E., Jungmann, F., Teiser, J., Schönau, L., & Wurm, G. (2021). Lifting of tribocharged grains by Martian winds. *Planetary Science Journal*, *2*(6), 238.

Laurent, S., Tobias, S., Jens, T., & Gerhard, W. (2021). Corona discharge of a vibrated insulating box with granular medium. *Granular Matter*, *23*, 68. https://doi.org/10.1007/s10035-021-01132-3.

Lee, V., Waitukaitis, S.R., Miskin, M.Z., & Jaeger, H.M. (2015). Direct observation of particle interactions and clustering in charged granular streams. *Nature Physics*, *11*(9), 733–737.

Liu, X., & Dong, Z. (2004). Experimental investigation of the concentration profile of a blowing sand cloud. *Geomorphology*, *60*(3), 371–381.

Loth, E. (2010). *Particles, Drops and Bubbles: Fluid Dynamics and Numerical Methods*. London, UK: Cambridge University Press.

Mallios, S.A., Daskalopoulou, V., & Amiridis, V. (2021). Orientation of non spherical prolate dust particles moving vertically in the earth's atmosphere. *Journal of Aerosol Science*, *151*, 105657.

Melnik, O., & Parrot, M. (1998). Electrostatic discharge in Martian dust storms. *Journal of Geophysical Research: Space Physics*, *103*(A12), 29107–29117.

Pähtz, T., Clark, A.H., Valyrakis, M., & Durán, O. (2020). The physics of sediment transport initiation, cessation, and entrainment across aeolian and fluvial environments. *Reviews of Geophysics*, *58*(1), e2019RG000679.

Park, G.I., Bassenne, M., Urzay, J., & Moin, P. (2017). A simple dynamic subgrid-scale model for LES of particle-laden turbulence. *Physical Review Fluids*, *2*(4), 044301.

Perot, J.B. (1993). An analysis of the fractional step method. *Journal of Computational Physics*, *108*(1), 51–58.

Rahman, M.M. (2020). *An investigation of electric fields in sandstorms* (PhD thesis, King Abdullah University of Science and Technology) Retrieved from http://hdl.handle.net/10754/667721.

Rahman, M.M., Cheng, W., & Samtaney, R. (2021). Generation and sustenance of electric fields in sandstorms. *Physical Review Research*, *3*(1), L012008.

Rahman, M.M., & Samtaney, R. (2017). Modeling and analysis of large-eddy simulations of particle-laden turbulent boundary layer flows. In *55th AIAA Aerospace Sciences Meeting*, Grapevine, TX (AIAA 2017-0981).

Sánchez-Lavega, A., Erkoreka, A., Hernández-Bernal, J., del Río-Gaztelurrutia, T., García-Morales, J., Ordoñez-Etxeberría, I., . . . Matz, K.D. (2022). Cellular patterns and dry convection in textured dust storms at the edge of Mars North Polar Cap. *Icarus*, *387*, 115183.

Sobrado, J.M., Martín-Soler, J., & Martín-Gago, J.A. (2015). Mimicking Martian dust: An in-vacuum dust deposition system for testing the ultraviolet sensors on the curiosity rover. *Review of Scientific Instruments*, *86*(10), 105113.

Spalart, P.R., Moser, R.D., & Rogers, M.M. (1991). Spectral methods for the Navier–Stokes equations with one infinite and two periodic directions. *Journal of Computational Physics*, *96*(2), 297–324.

Spiga, A. (2021). Turbulence in the lower atmosphere of Mars enhanced by transported dust particles. *Journal of Geophysical Research: Planets*, *126*(11), e07066.

Temel, O., Senel, C.B., Porchetta, S., Muñoz-Esparza, D., Mischna, M.A., Van Hoolst, T., . . . Karatekin, Ö. (2021). Large eddy simulations of the Martian convective boundary layer: Towards developing a new planetary boundary layer scheme. *Atmospheric Research*, *250*, 105381.

Temel, O., Senel, C.B., Spiga, A., Murdoch, N., Banfield, D., & Karatekin, O. (2022). Spectral analysis of the Martian atmospheric Turbulence: InSight observations. *Geophysical Research Letters*, *49*(15), 1–9.

Waitukaitis, S.R., Lee, V., Pierson, J.M., Forman, S.L., & Jaeger, H.M. (2014). Size-dependent same-material tribocharging in insulating grains. *Physical Review Letters*, *112*(21), 218001.

Witze, A. (2021). Lift off! first flight on Mars launches new way to explore worlds. *Nature*, *592*(7856), 668–669.

Wu, Z., Richardson, M.I., Zhang, X., Cui, J., Heavens, N.G., Lee, C., . . . Witek, M. (2021). Large eddy simulations of the dusty Martian convective boundary layer with MarsWRF. *Journal of Geophysical Research: Planets*, *126*(9), e2020JE006752.

Wurm, G., Schmidt, L., Steinpilz, T., Boden, L., & Teiser, J. (2019). A challenge for Martian lightning: Limits of collisional charging at low pressure. *Icarus*, *331*, 103–109.

Zhai, Y., Cummer, S.A., & Farrell, W.M. (2006). Quasi-electrostatic field analysis and simulation of Martian and terrestrial dust devils. *Journal of Geophysical Research: Planets*, *111*, E06016.

Zhang, H., Cui, Y., & Zheng, X. (2023). How electrostatic forces affect particle behaviour in turbulent channel flows. *Journal of Fluid Mechanics*, *967*, A8.

Zhang, H., Zheng, X.-J., & Bo, T.-L. (2014). Electric fields in unsteady wind-blown sand. *The European Physical Journal E*, *37*(2), 1–12.

Zhang, H., & Zhou, Y.H. (2020). Reconstructing the electrical structure of dust storms from locally observed electric field data. *Nature Communications*, *11*(1), 5072.

Zhang, H., & Zhou, Y.-H. (2023). Unveiling the spectrum of electrohydrodynamic turbulence in dust storms. *Nature Communications*, *14*(1), 408.

Zhang, H.F., Wang, T., Qu, J.J., & Yan, M.H. (2004). An experimental and observational study on the electric effect of sandstorms. *Chinese Journal of Geophysics*, *47*(1), 53–60.

Zhang, X., Li, D., & Bo, T.-L. (2018). The variation of the vertical electric field (E_z) with height during dust storms and the effects of environmental variables on E_z. *Granular Matter*, *20*, 1–10.

Zhou, Y.-H., He, Q.S., & Zheng, X.J. (2005). Attenuation of electromagnetic wave propagation in sandstorms incorporating charged sand particles. *The European Physical Journal E*, *17*(2), 181–187.